Research on Engineering Structures & Materials
www.jresm.org

Research Article

Microwave-assisted low-oxygen roasting–weak magnetic separation for desulfurization and iron enrichment from refractory high-sulfur iron tailings: A theoretical feasibility-domain analysis

Jigang Zhao [a], Enlei Wang [*,b]

School of Mining Engineering, University of Science and Technology Liaoning, Liaoning, China

Article Info

Article History:

Received 28 Aug 2026

Accepted 08 Oct 2026

Keywords:

Iron ore tailings;
Pyrite;
Magnetization roasting;
Microwave heating;
Desulfurization;
Thermodynamic modelling

Abstract

Refractory high-sulfur iron tailings are difficult to upgrade because desulfurization and magnetic enrichment require opposing oxygen environments. Oxidizing roasting removes sulfur as gaseous oxides but produces weakly magnetic hematite rather than magnetite. This strictly theoretical study, without experimental validation, redefines this incompatibility as a search for a common operating mode. Using measured Anshan tailings as the compositional matrix and a constructed high-sulfur condition as the reactive scenario, coupled thermodynamic, kinetic and mass-balance calculations define the temperature–oxygen-pressure window, bound magnetite conversion and iron recovery, and characterize the trade-off between desulfurization and magnetite yield. Desulfurization and magnetization occur within a narrow low-oxygen window, where pyrite-derived sulfur acts as an internal reductant converting hematite to magnetite, while microwave selective heating preferentially energizes reactive phases. The feasible band contracts sharply with increasing temperature. Magnetite-associated iron reaches 31.38 g per 100 g of feed, while the iron-recovery ceiling is 81.6%, with a realistic band of approximately 76–81%; these ceilings assume complete conversion of hematite and siderite without over-reduction, full use of the internal reductants (pyrite-derived S_2 and siderite-derived CO), and magnetic separation at the benchmark efficiency (0.12 T). The first roasting stage removes at most 42.9% of the sulfur; the remainder stays in magnetic pyrrhotite, and at least 95.6% of it must be removed in a second stage to bring the concentrate below 0.10% S. The results provide operating boundaries and performance expectations for subsequent engineering realization.

© 2026 MIM Research Group. All rights reserved.

1. Introduction

As the high-grade iron ore deposits become progressively more scarce, secondary sources of iron in solid waste have been utilized, and iron ore tailings from the Anshan mining base in China are a typical example of both large-scale accumulation and the demand for deep treatment of such waste [1]. Systematic evaluations have shown that these tailings contain a considerable amount of recoverable iron and some harmful impurities; however, their total utilization rate is low, which makes iron reclamation a resource and environmental imperative [2]. Magnetization roasting followed by low-intensity magnetic separation has become a leading reclamation route for such residues, and some designs are driven by pyrolytic reducing gas [3] or biomass-derived reductants that reduce reliance on fossil carbon [4]. Among the candidate resources, a particular problem exists in the form of refractory high-sulfur tailing; its magnetic response is close to that of magnetite, so beneficiation alone rarely reduces the concentrate sulfur to an acceptable level, and

*Corresponding author: enlei_wang@outlook.com
[a]orcid.org/0009-0002-2593-7185; [b]orcid.org/0000-0002-9026-6923
DOI: http://dx.doi.org/10.17515/resm2026-2269vk0828rs

downstream ironmaking suffers from hot shortness [5]. Sulfur contents above about 0.05% in iron concentrates cause steel brittleness and reduced weldability, and concentrate sale contracts typically tolerate no more than about 0.1% S [6]; the Anshan benchmark concentrate used in this study contains 0.063 wt% S [7].

A fundamental obstacle underlies this difficulty. Sulfur removal is generally carried out by oxidizing roast; sulfur is released as gaseous oxides from refractory sulfur-bearing ores, and hematite is left behind because it is thermodynamically favorable [8]. Efficient low-intensity magnetic separation requires the strongly magnetic magnetite phase obtained under reducing conditions [9]. Therefore, the two goals require different oxygen environments. Routes for phase-transformation that simultaneously aim to reduce sulfur and recover iron have succeeded, but they require a hydrogen-based reducing atmosphere [10], and magnetization routes that supply external CO or H_2 incur extra reagent costs and process difficulties [11]. For the present feed, stoichiometric reduction of the hematite ($3Fe_2O_3 + H_2 \rightarrow 2Fe_3O_4 + H_2O$) needs 1.29 kg of H_2 per tonne; at 20–50% utilization and an illustrative US$2–6 kg^{-1}, the reductant alone costs US$5–39 t^{-1}, excluding storage, recirculation and safety costs. The internal-reductant route needs no purchased reductant but must control a narrower oxygen window and treat a sulfur-bearing off-gas (Section 4). This oxygen-atmosphere conflict has rarely been considered as a combined constraint, and thus, any single-stage desulfurization–magnetization route must meet this design space.

Two developments make a reconciled route conceivable. Microwave irradiation heats the absorbing sulfide and iron-oxide phases more readily than the relatively transparent silicate gangue, concentrates energy on the reactive phases, and thus reshapes the local reaction pathway rather than increasing the overall temperature [12]. Beyond heating, the differential thermal expansion between absorbing and transparent grains induces micro-cracking along grain boundaries, which has been reported to lower grinding energy and to enhance mineral liberation [13]. Regardless of the heating method, the thermal decomposition of pyrite in an oxygen-deficient environment releases reactive sulfur species [14], and the resulting reduction of hematite to magnetite can be limited, along with the suppression of over-reduction, to a narrow low-oxygen window defined by the iron–sulfur–oxygen stability relationship [15]. It is unknown whether desulfurization and magnetization can be realized simultaneously in a single operating mode, and if so, how far such a mode can be applied before over-reduction or residual sulfur remains.

Therefore, a model and feasibility-domain analysis have been carried out in this paper instead of experimental optimization. As the compositional matrix and a given high-sulfur condition as the reactive scenario [16] are taken from a measured Anshan tailing, the work couples an iron–sulfur–oxygen thermodynamic stability description with a closed mass-balance treatment to determine the operable temperature–oxygen-pressure window, to limit the attainable magnetite conversion and iron recovery, and to characterize the trade-off between further desulfurization and magnetite yield. The rate-limiting first desulfurization step is a scheme of oxygen-free shrinking-core thermal decomposition, and the magnetization path is restricted by the reduction of hematite and the concurrent decomposition of siderite in similar roasting systems [17]. All quantitative results are in the form of model-calculated values or theoretical limits, and absolute times are given only as order-of-magnitude estimates anchored to a published rate measurement, and no experimental validation is included. Thus, the contribution is an original theoretical system that indicates where the coupled process can operate and how efficient it can be in principle, providing boundary criteria for subsequent engineering realization.

2. Data and Methods

2.1 Representative High-Sulfur Iron Tailing as Model Input

The compositional matrix of this study is based on a measured Anshan iron ore tailing with a total iron content of 33.19 wt% and a gangue that is mainly silica, with some alumina, lime and magnesia. The iron exists in several forms: hematite, primary magnetite, carbonate (siderite), and silicate-locked phases; the silicate-locked fraction is non-magnetic and thus not recovered by magnetic separation. Due to the low sulfur content of the Anshan resource, it is not classified as a high-sulfur area in the measurement results; instead, a model for a high-sulfur feed material was constructed

by adding pyrite to the measured matrix and renormalizing the composition to reach a sulfur content of 2.0 wt%, in line with the pyrite-plus-hematite mineralogy and roasting behavior reported for genuine high-sulfur iron ores. The resulting two-column feed has the real tailing on one side and the constructed high-sulfur model feed on the other; it fixes the elemental and phase inputs used in the analysis and is summarized in Table 1. The model feed has 0.50 percentage points more TFe than the real tailing (33.69% vs. 33.19%) only because the added pyrite (3.89 g FeS_2 per 100 g of tailing, i.e., 3.74 wt% FeS_2 and 1.74 wt% Fe in the model feed) supplies iron while diluting the other components by 1/1.0389. The iron-phase distribution (22.22, 4.64, 5.73 and 0.60 wt% Fe in hematite, magnetite, siderite and silicates) is taken from Yu et al. and renormalized likewise; the 0.05 wt% background sulfur is neglected. In the constructed feed all sulfur is pyrite; the implications for real tailings are discussed in Section 4.

Table 1. Composition of the High-Sulfur iron tailing feed (Model Input)

Component	Real Anshan tailing	Model high-S feed
TFe (%)	33.19	33.69
S (%)	0.05	2.00 (as FeS_2, constructed scenario)
SiO_2 (%)	41.19	39.65
Al_2O_3 (%)	1.82	1.75
CaO (%)	1.77	1.70
MgO (%)	1.78	1.71
Fe in hematite, % (Fe_2O_3, wt%)	22.22 (31.77)	21.39 (30.58)
Fe in magnetite, % (Fe_3O_4, wt%)	4.64 (6.41)	4.47 (6.17)
Fe in siderite, % ($FeCO_3$, wt%)	5.73 (11.89)	5.52 (11.44)
Fe in silicates, %	0.60	0.58
Fe in pyrite, % (FeS_2, wt%)	—	1.74 (3.74)

2.2 Coupled Desulfurization–Magnetization Framework Under Low Oxygen Partial Pressure

The three reactions occur in a single, low-oxygen window and are thus not treated as separate oxidation and reduction steps. Pyrite thermally decomposes to release sulfur; the liberated sulfur species reduce hematite to magnetite, and siderite decomposes into magnetite; thus, when the oxygen partial pressure is within the field bounded by the iron–sulfur–oxygen stability relations, desulfurization and magnetization become coupled. Microwave irradiation serves as a selective heating method to concentrate energy on the absorbing sulfide and iron-oxide phases, leaving the transparent silicate gangue relatively cool; qualitatively, this effect is treated as such, and a model variable of temperature is used instead of applied power. The entire computational logic of the feed definition, thermodynamic and mass-balance modules, bounded performance indicators, etc., is shown in Figure 1. The absorbed power density is $P = 2\pi f \varepsilon_0 \varepsilon'' E^2$ and the penetration depth $D_p = c/\{2\pi f[2\varepsilon'((1 + \tan^2\delta)^{1/2} - 1)]^{1/2}\}$ [18]. At 2.45 GHz sulfide minerals have $\varepsilon'' \approx 1–12$ and dry quartz-rich materials $\varepsilon'' \approx 0.0075–0.32$ [19], so the absorbing phases are assigned $\varepsilon'' = 0.1–10$. For a grain of radius r in a matrix of conductivity $k \approx 1.5$ W m^{-1} K^{-1}, the grain-to-matrix overtemperature $\Delta T \approx Pr^2/(3k)$ is ≤ 1.5 K for $r_0 = 20$ μm, $\varepsilon'' \leq 10$ and $E \leq 10^5$ V m^{-1} (relaxation time ≈ 0.4 ms), so the isothermal treatment is retained. Selective heating matters at the agglomerate and bed scale (10^1–10^3 K for 1 mm absorber-rich clusters) and is represented by an effective overtemperature ΔT_{eff} = 0–50 K (Sections 3.1 and 3.2).

2.3 First-stage Desulfurization Kinetics

The rate-limiting step is the thermal decomposition of pyrite to pyrrhotite, which, under an oxygen-starved condition, is independent of oxygen partial pressure and thus expressed in an oxygen-free shrinking-core model rather than an oxidative rate law. The two regimes are gas-film heat-transfer control at low conversion (X ≤ 0.35 in Figure 3) and product-layer diffusion control at high

conversion, and the corresponding activation energies are taken as 113 and 96 kJ·mol^{-1}. A reference particle radius of 20 μm is used, with a sensitivity range of 10–40 μm. Reported activation energies for pyrite decomposition vary considerably in the literature [20], and the present work incorporates this scatter as an extended sensitivity range around the shrinking-core value rather than using any single external figure. For a sphere of radius r_0, $t = \tau_f X$ under gas-film control and $t = \tau_d[1 - 3(1 - X)^{2/3} + 2(1 - X)]$ under product-layer diffusion control, with $\tau_f = \rho_B r_0/(3bk_gC)$ and $\tau_d = \rho_B r_0^2/(6bD_eC)$; hence $k_g \propto r_0^{-1}$ and $k_d \propto r_0^{-2}$. As pre-exponential factors are not reported by Boyabat et al., τ_f and τ_d are anchored separately to the isothermal data of Aracena and Jerez (87% of the $FeS_2 \rightarrow Fe_7S_8$ mass loss in 520 s at 550 °C, r_0 = 8 μm), so the two regimes bracket the mixed-control time; as these data were obtained under 5.07 kPa O_2, these are lower-bound times for an inert gas. Size distribution is included by integrating over a Rosin–Rammler distribution, $F(d) = 1 - \exp[-(d/d_{63.2})^n]$, with $d_{63.2}$ = 40 μm and n = 0.9–1.2, and over the benchmark feed (77% passing 38 μm). The stoichiometry of pyrite-to-pyrrhotite conversion limits the first-stage desulfurization at a certain fraction, and further sulfur removal requires the second-stage treatment quantified in Section 3.5 rather than by extending this single-stage rate.

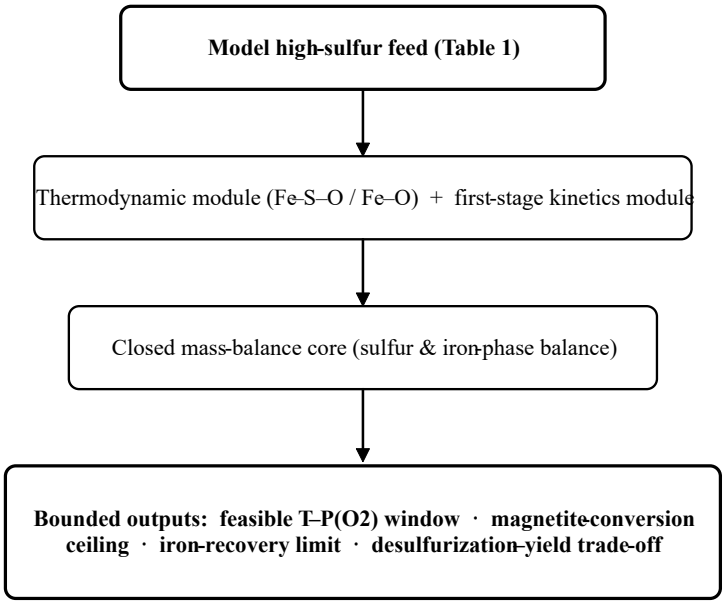


Fig. 1. Computational flow of the feasibility analysis

2.4 Thermodynamic Criteria for Magnetization

The magnetization path is constrained by the Fe–S–O and Fe–O stability relations; thus, a low-oxygen window exists where magnetite is stable, and outside this window, either hematite is formed or over-reduction to wüstite and metallic iron occurs. Sulfur-mediated reduction converts hematite into magnetite in this window and is written with the dominant vapor species S_2(g), $S_2(g) + 12Fe_2O_3 \rightarrow 8Fe_3O_4 + 2SO_2$, and siderite decomposes into magnetite via a two-step carbonate pathway typical of analogous flowing-atmosphere systems. The CO released by siderite also reduces hematite ($CO + 3Fe_2O_3 \rightarrow 2Fe_3O_4 + CO_2$), so the whole gas phase (p_{CO}, p_{CO2}, p_{S2}, p_{SO2}, p_{COS}) is coupled to the oxygen potential through $CO + ½O_2 = CO_2$, $½S_2 + O_2 = SO_2$ and $CO + ½S_2 = COS$. Standard Gibbs free energies of formation of Fe_2O_3, Fe_3O_4 and FeO at 700–1000 K are taken from the NIST-JANAF thermochemical tables and linearly interpolated, the gas species are evaluated with the NASA Glenn coefficients [21] via the open-source Cantera library (agreement within 0.03 log units), and all calculations use custom MATLAB and Python scripts without FactSage or HSC Chemistry (ΔG°–T relations in Tables S1 and S2). The resulting equilibrium boundaries are used to define the operating region rather than to predict conversion at a particular condition.

2.5 Mass-Balance Boundaries and Theoretical-Limit Calculations

The first part is a closed-system material balance based on 100 g of feed. The sulfur balance splits the initial sulfur into gaseous escape and solid residue, $n_{S,0} = n_{S,gas} + n_{S,res}$ with $n_{S,res} \geq 0$, and the iron-phase balance expresses the magnetite-associated iron as $m_{Fe,mag} = m_{Fe,Mt} + X_C m_{Fe,Sd} + X_H m_{Fe,Hm} -$

L_{over}, with $0 \le X_C, X_H \le 1$ and $L_{over} \ge 0$, capped at the material ceiling set by the reducible inventory. The reductant budget, the magnetite-conversion ceiling, the iron-recovery limit, and the concentrate-grade and impurity-rejection anchors are all derived from these balances, and the separation efficiency is set at the liberation and fines-loss factor implied by the iron recovery reported for the Anshan benchmark. To resolve the field dependence, $\eta_{sep} = \lambda R_{cap}(B)$, where $\lambda = 0.90$ is an assumed liberation factor and $R_{cap}(B)$ is the mass fraction of liberated magnetic grains coarser than $d_c = [18\eta v\mu_0 L_g/(\chi B^2)]^{1/2}$, the size at which the magnetic force density $\chi B^2/(\mu_0 L_g)$ balances Stokes drag (product 95% passing 38 μm). The slurry velocity v is calibrated to $\eta_{sep} = 0.83$ at 0.12 T, with $\chi = 1.0$ (magnetite), 0.05–0.3 (monoclinic pyrrhotite) and 0.003 (hematite) [22,23]. Gangue entrainment is described by a coefficient e, calibrated to 0.129 from the benchmark grade of 61.37% TFe. The model parameters and settings are shown in Table 2, and all derived indicators are either model-calculated values or theoretical limits.

Table 2. Model parameters and settings

Parameter	Value	Source
First-stage desulfurization reaction	anoxic thermal decomposition, 7FeS2 → Fe7S8 + 3S2(g)	Boyabat et al.
Kinetic model	shrinking-core: gas-film control (low X) / ash-layer diffusion (high X)	Boyabat et al.
Activation energy Ea	113 kJ·mol−1 (gas-film) / 96 kJ·mol−1 (ash-layer)	Boyabat et al.
Ea sensitivity band	96–350 kJ·mol−1 (literature scatter)	Hu et al. (sensitivity setting)
Particle radius r0	20 μm (sensitivity 10–40); kg ∝ r0−1, kd ∝ r0−2	shrinking-core geometry
Oxygen partial pressure pO2	no pO2 term in desulfurization rate; low pO2 sets magnetization feasibility	Aracena and Jerez
Magnetization / decomposition reactions	S2(g) + 12Fe2O3 → 8Fe3O4 + 2SO2; 3FeCO3 → Fe3O4 + 2CO2 + CO; CO + 3Fe2O3 → 2Fe3O4 + CO2	Aracena and Jerez; Zhu et al.
Temperature / time (variables)	500–700°C / 10–30 min	model variables
ΔG–T data	NIST-JANAF (Fe2O3, Fe3O4, FeO); NASA Glenn (CO, CO2, S2, SO2, COS); custom MATLAB/Python scripts	NASA Glenn; Tables S1–S2
Absolute time anchor	X = 0.87 in 520 s at 550 °C, r0 = 8 μm (FeS2 → Fe7S8)	Aracena and Jerez
Particle-size distribution	Rosin–Rammler, d63.2 = 40 μm, n = 0.9–1.2; benchmark feed	Yu et al. / assumed
Microwave parameters	f = 2.45 GHz; ε″ = 0.1–10; E ≤ 105 V m−1; ΔTeff = 0–50 K	Section 2.2
Magnetic separation	B = 0.08–0.30 T (benchmark 0.12 T); λ = 0.90; e = 0.129	Section 2.5; λ assumed

3. Results

3.1 Thermodynamic Feasibility Domain of the Coupled Process

The operating region is obtained by intersecting the requirements for desulfurization, magnetization and suppression of over-reduction on a single temperature–oxygen-pressure plane. The upper bound for oxygen partial pressure is set by the smaller of the hematite-magnetite equilibrium and the low-oxygen limit where pyrite decomposition occurs; thus, magnetite rather than hematite is the stable oxide, and its lower bound is the magnetite-wüstite boundary, below which reduction to wüstite and metallic iron begins. From 500 to 700 °C, the feasible band contracts

sharply; that is, from about nine orders of magnitude at the low-temperature end to less than three at 700 °C, because the reducing boundary rises more rapidly than the oxidizing boundary. A representative interior oxygen pressure near $\log_{10}(p_{O2}/p°$, $p° = 1$ bar) of −18 falls within the common domain of all sampled temperatures and retains only a narrow margin at the extremes; thus, the coupling is governed by the intersection of the sulfur-release field and the magnetite-stability field rather than by an unlimited reduction of oxygen pressure, in line with the atmosphere requirements reported for neutral and low-oxygen magnetization systems [24]. The Feasible Region is shown in Figure 2. At 700 °C the window spans only 2.76 decades (−16.00 to −18.76), i.e., p_{CO2}/p_{CO} = 17–417 or 0.2–5.4% CO in CO + CO_2, against 6.28 decades (p_{CO2}/p_{CO} = 17 to 2.3 × 10^4) at 600 °C. The magnetite–wüstite boundary moves by 0.031-decade K^{-1} near 700 °C, so a ±10 K excursion or overtemperature consumes 11% of the 700 °C window and 50 K more than half of it; the −18 set-point keeps margins of only 0.76 decade (700 °C) and 0.05 decade (500 °C). Temperatures of 600–650 °C (4.4–6.3 decades) are therefore preferred. The Fe–S–O limit of −16 is a conservative, temperature-independent bound; a temperature-dependent limit would only widen the window at high temperature (Table S2).

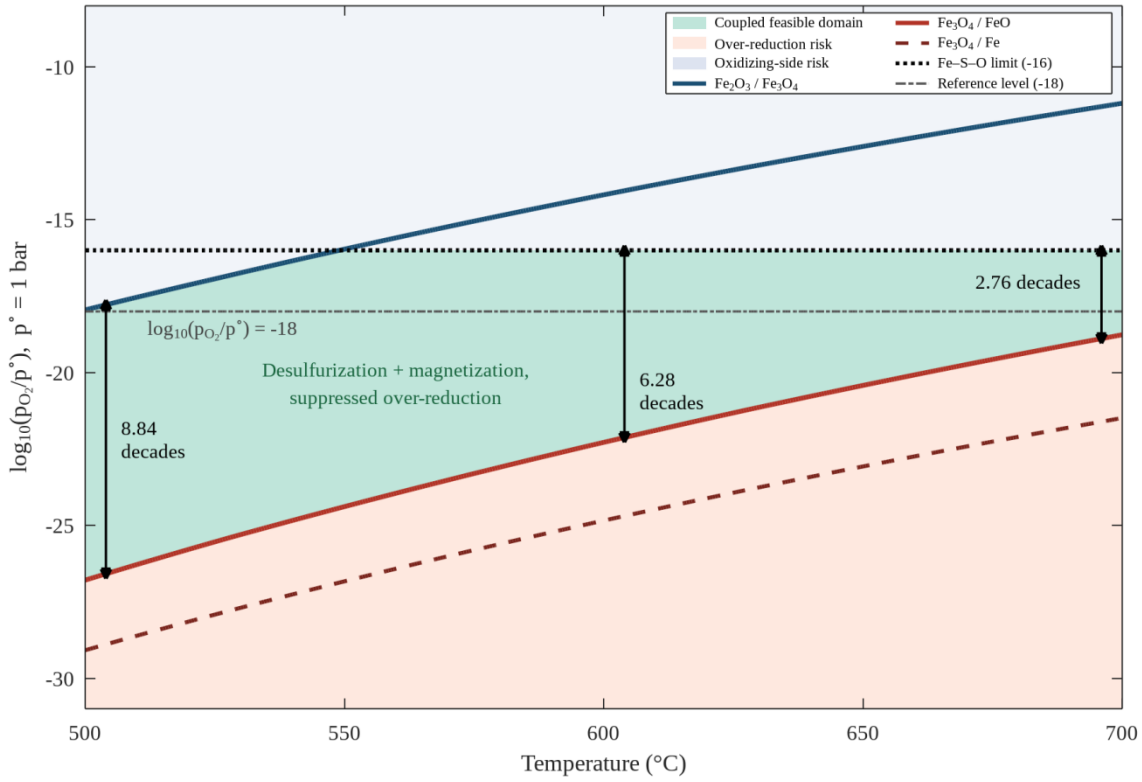


Fig. 2. Thermodynamic feasibility domain (model calculation)

3.2 Kinetics of the First Desulfurization Stage

The rate behavior of the controlling first stage is shown in normalized form relative to a standard condition (600 °C, r_0 = 20 μm), and the anchored absolute time scale is given on the top axes of Figures 3a and 3b. The temperature dependence follows an Arrhenius relationship, and at 500–700 °C, the relative rate is more than an order of magnitude higher; for a gas-film-controlled energy of 113 kJ·mol^{-1}, it increases by about 40 times, and for a diffusion-controlled energy of 96 kJ·mol^{-1}, it increases by about 20 times. The particle-radius dependence follows shrinking-core geometry, so the gas-film-controlled rate scales inversely with radius and the diffusion-controlled rate inversely with its square, which makes the high-conversion stage the more sensitive to grind size. Reported activation energies for pyrite decomposition have a large scatter, and propagating this scatter as a sensitivity band broadens the spread of relative times without changing the qualitative order. Therefore, the relative time to reach the first-stage endpoint will be shorter at higher temperatures. That endpoint is inherently limited because the pyrite-to-pyrrhotite stoichiometry

releases no more than three-sevenths of the sulfur, about 42.9%, so further sulfur removal must be achieved through the subsequent thermodynamically controlled step rather than extended first-stage roasting. With this anchoring, the 90% conversion time t_{90} of 20 μm pyrite is about 9 min (film) to 27 min (diffusion) at 600 °C, 2–7 min at 700 °C and 65–150 min at 500 °C (Figure 3f). A Rosin–Rammler distribution ($d_{63.2}$ = 40 μm) lengthens t_{90} at 600 °C to 11–38 min (n = 1.2) or 13–52 min (n = 0.9), and t_{99} under diffusion control to about 200 min, because the coarsest 10% of the mass keeps unreacted cores (Figure 3e); the finer benchmark feed gives 8–18 min. An overtemperature of 10, 25 or 50 K accelerates the first stage about 1.2, 1.5 or 2.2 times, within the uncertainty of the anchored times. The kinetics are shown in Figure 3.

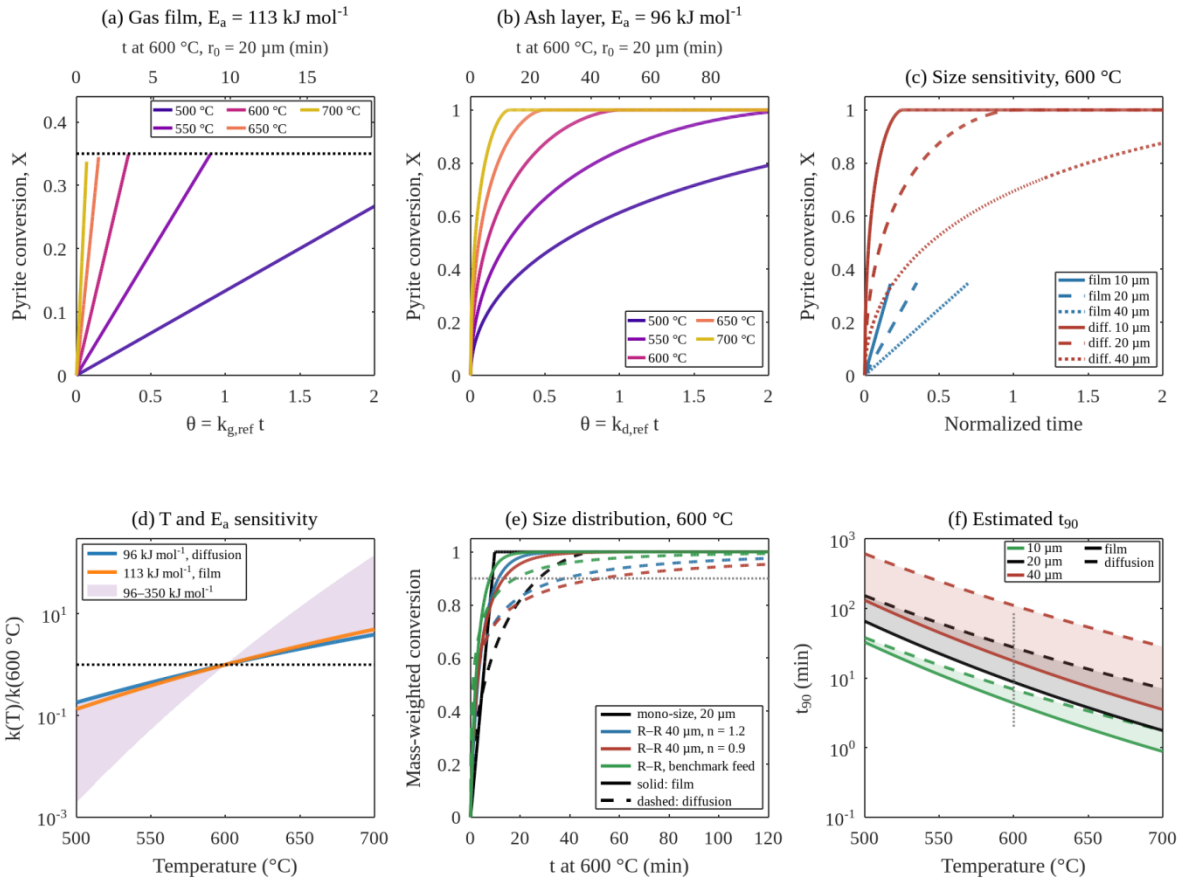


Fig. 3. First-stage desulfurization kinetics (model calculation)

3.3 Material Boundary of Magnetite Conversion

The magnetite-associated iron is represented as a linear combination of primary magnetite, siderite-derived iron and sulfur-reduced hematite, with no over-reduction loss, and is thus a monotonically increasing function of the hematite-magnetization and siderite-decomposition fractions. Siderite contribution follows the established decomposition of carbonate to magnetite under low-oxygen roasting [25,26], and evaluation of the four corners of the conversion plane shows that the material ceiling for magnetite iron per 100 g of feed is 31.38 g, reached only when both fractions equal unity without over-reduction. Because both partial derivatives are positive, this ceiling is a single corner rather than a line across the plane, and over-reduction can only lower the magnetite iron, which is consistent with the loss of iron to fayalite and spinel phases observed when reduction is carried out too far [27], e.g., $Fe_3O_4 + CO \rightarrow 3FeO + CO_2$ and $2FeO + SiO_2 \rightarrow Fe_2SiO_4$ (overall $2Fe_3O_4 + 3SiO_2 + 2CO \rightarrow 3Fe_2SiO_4 + 2CO_2$). Silicate-locked iron (0.58 g per 100 g) is excluded because iron-bearing silicates do not transform to magnetite at 500–700 °C under low oxygen potential; it stays paramagnetic, is not captured by LIMS, and even rises slightly on roasting the benchmark feed (0.60 to 0.71 wt% Fe). The sulfur-containing iron added via pyrite is accounted for separately and thus not included in the ceiling height calculation twice. According to the budget

check, about 0.0319 mol of sulfur (0.0160 mol S_2) is required to reduce the entire hematite inventory. Of the 0.0624 mol of sulfur in the feed, the first stage releases only three-sevenths, 0.0267 mol (0.0134 mol S_2), covering 83.8% of the demand ($X_H \leq 0.838$, dashed line in Figure 4). The remaining 16.2% is met by siderite-derived CO: 0.0988 mol $FeCO_3$ yields 0.0329 mol CO ($3FeCO_3 \rightarrow Fe_3O_4 + 2CO_2 + CO$), three times the 0.0104 mol needed, and the p_{CO2}/p_{CO} ratios in the window (17 to 2.3×10^4) ensure its consumption. The internal reductants thus supply 0.0864 mol of oxygen-removal capacity against a demand of 0.0638 mol, so the binding constraint remains the reducible iron inventory rather than the reductant, in line with self-magnetization roasting driven by an internal reductant [28]; without the siderite CO, complete conversion within the first stage would not be possible. COS is negligible inside the window ($p_{COS}/p_{CO2} \approx 3 \times 10^{-4}$ at 600 °C, −18 and $p_{S2} = 10^{-3}$ bar) and reaches only 1–4% of the carbon at the reducing boundary (600–700 °C); sulfur leaves mainly as SO_2 near the upper and as S_2 near the lower bound. The material feasibility surface and its ceiling are shown in Figure 4.

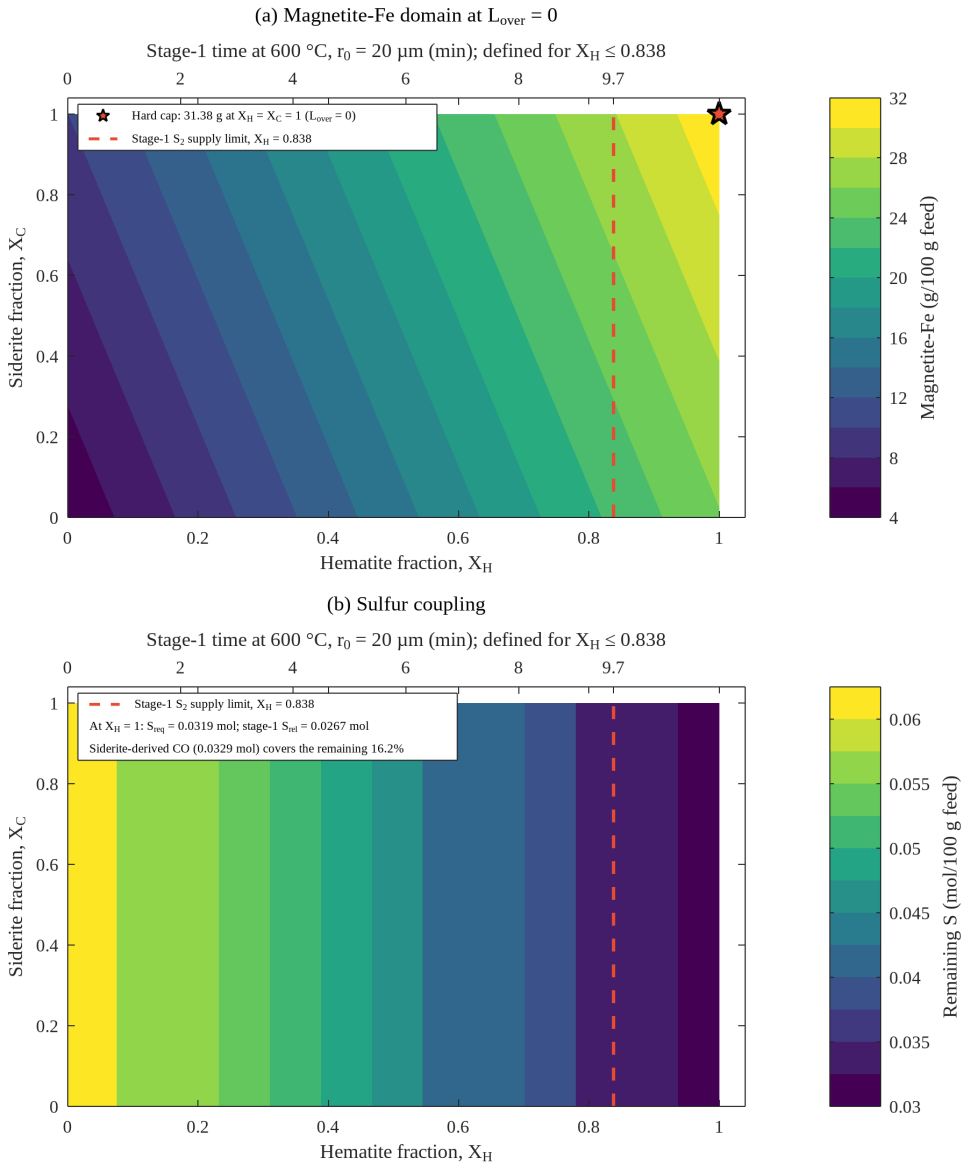


Fig. 4. Material feasibility surface for magnetite conversion (model calculation)

3.4 Theoretical Limits of Recovery and Grade

The iron-recovery limit is determined by the magnetite ceiling, separately tracked sulfide-derived iron, and a fixed liberation-and-fines-loss factor at the Anshan benchmark. Propagating this term puts the recovery ceiling at 81.6%, with a reasonable band of about 76–81%, and this figure is

reported as calculated rather than adjusted to a target; it is about 0.2 percentage points lower than the recovery reported for comparable Anshan feed, which supports the internal consistency of the accounting and does not exceed the benchmark. The concentrate grade is based on the reference separation condition of 58–61% total iron against a benchmark of 61.4%, not predicted for every operating point, and impurity rejection is shown by a reduction in silica from 41.19% to about 10.24% and in alumina from 1.82% to about 0.88% established for the benchmark concentrate, consistent with the grades obtained in magnetizing-roasting and separation practice on similar ores. The residual sulfur in the unconverted pyrrhotite is included in the concentrate account, as this phase is magnetic and reported with magnetite. Theoretical upper bounds are shown in Table 3. At 0.12 T the critical capture diameter is about 1.9 μm for magnetite, 3.4–8.4 μm for monoclinic pyrrhotite and 34 μm for hematite. Across 0.08–0.30 T the recovery bound varies from 77.6% to 86.1%, but higher fields also raise pyrrhotite capture from 61–85% (0.12 T) to 85–95% (0.30 T) and floc entrainment, so the benchmark value is kept as the reference ceiling. The grade is more sensitive to entrainment than to field: e = 0.05–0.25 gives 67.7–53.7% TFe, and the 58–61% band corresponds to e ≈ 0.13–0.18.

Table 3. Theoretical limits and reference anchors (Model-calculated Values)

Indicator	Theoretical limit / range	Note
Iron-recovery ceiling	81.6 %	≈ benchmark 81.8%; see footnote [a]
Realistic iron-recovery band	ca. 76–81 %	theoretical boundary range, not a target
Concentrate TFe grade	58–61 %	benchmark: 61.4 %
Impurity rejection (concentrate)	SiO_2 → ~10.24 %, Al_2O_3 → ~0.88 %	benchmark anchors
Magnetite-Fe material ceiling	≤ 31.38 g/100g	primary + siderite + reducible hematite
First-stage residual sulfur	~1.143 g S/100 g (magnetic Fe_7S_8)	concentrate S ≈ 2.3% if untreated; D_2 ≥ 0.956 needed for ≤ 0.10% S
Iron recovery vs. field strength	77.6–86.1 % (0.08–0.30 T)	λ = 0.90; field-dependent capture, Section 2.5

[a] *(31.38 + 1.75) × 0.83 / 33.69 × 100% = 81.6%; 1.75 g is pyrite-derived iron reporting as magnetic sulfide and 0.83 the separation factor at 0.12 T.*

3.5 Trade-Off Between Second-Stage Desulfurization and Magnetite Yield

The conflict between low concentrate sulfur and high magnetite yield is that the first stage locks a large proportion of the sulfur into magnetic pyrrhotite, leaving about 1.143 g of sulfur per 100 g of feed in that phase after the first stage is completed, and this residue reports with the concentrate unless a further removal step is taken. That step requires more severe conditions and risks crossing the reducing boundary shown in Figure 2, thus losing magnetite through over-reduction. Expressing the concentrate residual sulfur as a decreasing function of the second-stage removal extent and the recovery as a decreasing function of the over-reduction loss defines a boundary envelope rather than a single operating curve, because the coupling between removal extent and over-reduction is not fixed by any available rate function. The formal corner at which residual sulfur vanishes, magnetite reaches its ceiling, and over-reduction is nil cannot be demonstrated to be simultaneously achievable; therefore, it is designated as an excluded limit rather than an operating point. Therefore, the reasonable operation will advance the second stage in the intersection of the sulfur-release field and the magnetite-stability field, maintaining a margin away from the reducing boundary. Because monoclinic pyrrhotite reports to the magnetic concentrate (Section 3.4), the untreated stage-1 residue would give 1.4–2.0% S at the capture calculated for 0.12 T, or 2.2–2.3% S under the conservative 95% capture used below, far above the tolerated 0.05–0.1% S. As concentrate sulfur scales with $(1 - D_2)$, the second stage must remove at least 86.9%, 93.5%, 95.6% and 97.8% of the pyrrhotite sulfur to reach 0.30%, 0.15%, 0.10% and 0.05% S (D_2 ≥

0.93–0.95 suffices for 0.10% S at 0.12 T capture). Keeping recovery within 76–81% further requires $L_{over} \leq 2.28$ g Fe per 100 g, so the admissible region is the corner $D_2 \geq 0.956$, $L_{over} \leq 2.28$ g (Figure 5b). Whether a real second stage reaches it depends on the unknown $L_{over}(D_2)$; desulfurization is therefore claimed only as the first-stage limit plus a quantified second-stage requirement. The trade-off envelope is shown in Figure 5.

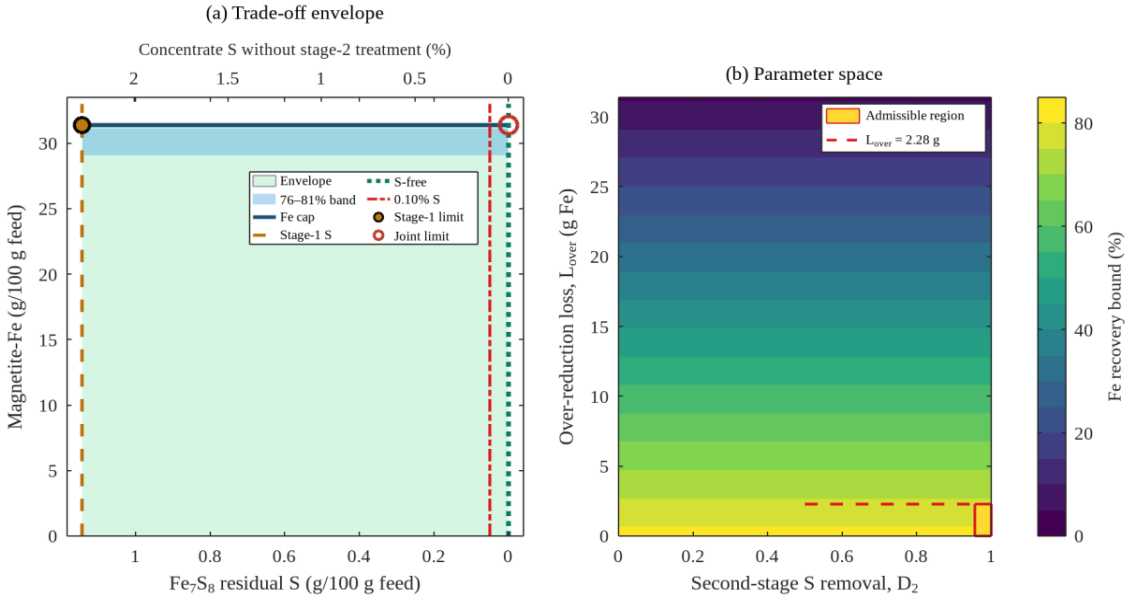


Fig. 5. Trade-off between second-stage desulfurization and magnetite yield (model calculation)

4. Discussion

Based on the above analysis, it can be concluded that the long-standing incompatibility between sulfur removal and magnetic enrichment is not an intrinsic contradiction but rather the result of operating in an unsuitable oxygen-potential region. The traditional oxidation route promotes the formation of a sulfide phase that is difficult to separate magnetically, as well as gaseous sulfur oxides; therefore, sulfur is lost and a magnetic response cannot be obtained, requiring external supply of CO or H_2 for reduction. By placing desulfurization and magnetization in the same low-oxygen environment, this study has found that the sulfur released during the decomposition of pyrite can act as a reducing agent to transform hematite into magnetite; thus, both aims can be achieved by regulating the atmosphere without adding other chemicals. The selective heating characteristic of microwave irradiation is a natural complement to this scheme; that is to say, it concentrates energy on the absorbing sulfide and oxide phases while keeping the transparent silicate gangue relatively cool, and microwave-assisted magnetization roasting can reduce the roasting time and lower the required temperature compared with conventional heating [29], and the broader body of microwave mineral-processing work attributes such gains to volumetric and phase-selective heating rather than to any change in the underlying thermodynamics.

Framing the problem as a feasibility domain is advantageous because it can demonstrate the application scope of the process and how far it can be promoted before controlling constraints take effect. The narrowing of the operable band with an increase in temperature indicates that aggressive heating achieves faster kinetics but at the expense of a reduced margin against over-reduction; the same internal-reductant logic must still be met. The recovery ceiling near the value reported for comparable Anshan feed, obtained without adjusting the loss factor to a target, suggests that the coupled route is capable of matching the established performance of such feed rather than exceeding it; thus, it is a more defensible claim than an optimistic projection would allow. This position is in line with the grades and rejection rates of magnetizing-roasting and separation practice for similar ores. The problem of trade-off between further desulfurization and magnetite yield is the practical bottleneck, as the sulfur remaining in magnetic pyrrhotite reports

with the concentrate, and reducing it further requires conditions that approach the reducing boundary and sacrifice iron for over-reduced phases.

Figure 6 outlines the route: microwave furnace under an N_2 sweep, gas separator, inert cooling and regrinding, low-intensity magnetic separation (LIMS) and second-stage treatment of the magnetic concentrate. The 1.143 g S per 100 g retained in pyrrhotite can be removed by a mildly oxidizing low-temperature stage converting Fe_7S_8 to Fe_3O_4, which must avoid re-forming hematite and thus carries the L_{over} risk, or by pyrrhotite flotation from the magnetic concentrate with xanthate collectors, whose selectivity depends on the pyrrhotite superstructure and surface oxidation [30]. Flotation acts after LIMS without disturbing the magnetite and is the lower-risk way to reach $D_2 \geq 0.956$.

The first stage releases 8.6 kg S t^{-1} (17.1 kg SO_2 t^{-1} if fully oxidized) as S_2 and SO_2. Sulfur vapor sulfides steels and Ni alloys, and SO_2/SO_3 condensing below the acid dew point corrodes ducts, cavity and waveguides, so ceramic-lined internals, N_2-purged windows and heated off-gas lines are needed; elemental sulfur can be condensed, whereas the dilute SO_2 requires enrichment, scrubbing or an existing acid plant [31]. The theoretical heat demand is about 670 MJ t^{-1} (186 kWh t^{-1}; 544 MJ sensible heat to 600 °C plus 126 MJ reaction heat). With magnetron efficiencies of 85% (915 MHz) to 50% (2.45 GHz) [32] and 0.8 coupling efficiency, the electricity demand is 270–470 kWh t^{-1}, i.e., 2.4–4.2 GJ t^{-1} of primary energy at 40% generation efficiency, against 1.3–2.2 GJ t^{-1} of fuel for a rotary kiln at an assumed 30–50% efficiency. Microwave heating is thus not cheaper for bulk heating; its benefit is selective, rapid heating and atmosphere control, and conventional preheating with microwave finishing plus calcine heat recovery is the logical compromise.

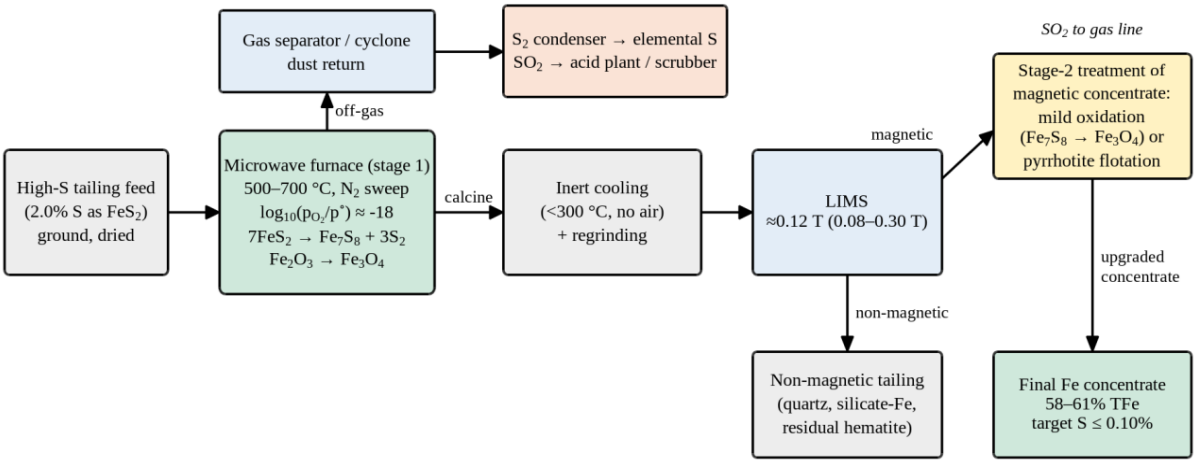


Fig. 6. Conceptual block flow diagram

Several limitations bound these conclusions and mark directions for further work. First-stage absolute times are anchored to a single published measurement made in a weakly oxidizing gas, so they are order-of-magnitude estimates; the analysis mainly demonstrates how the rate changes with temperature and particle size. The connection between the second-stage sulfur removal and over-reduction loss is left as an envelope rather than a curve because no validated rate function has been established for this relationship, and resolving it would require dedicated kinetic measurements of the pyrrhotite-to-oxide step under controlled low-oxygen atmospheres of the kind used for siderite-bearing systems [33]. Idealization of precise oxygen control should also be subjected to scrutiny, as industrial realization may still require a supplementary reducing agent to maintain the atmosphere within the feasible range, such as in the suspension route for refractory ores where a reducing gas is generally added [34], and the compositional matrix here is a constructed high-sulfur feed based on measured low-sulfur tailing rather than sampled high-sulfur material. Real tailings, unlike this synthetic feed, also contain pyrrhotite ($Fe_{1-x}S$), which releases little S_2 and reports to the magnetic concentrate, marcasite, which behaves like pyrite, sulfates that stay as non-magnetic sulfur, and flotation reagents that add reductant; the limits derived here therefore apply to pyrite-dominated feeds. At industrial scale, standing waves create hot and cold zones, and the 2.45 GHz penetration depth falls from 0.3–1.3 m for quartz-rich bulk to 0.02–0.12 m

once absorbers raise ε″ to 0.3–3 (about 2.7 times larger at 915 MHz); as loss factors rise with temperature, thermal runaway could consume much of the narrow high-temperature window (Section 3.1), so thin moving or fluidized beds, mode stirring and 915 MHz sources are needed. These constraints do not negate the main result; that is, a single low-oxygen environment can theoretically achieve first-stage desulfurization and efficient magnetite generation, but it is only a theoretical concept to date, requiring quantification of second-stage kinetics and stable-atmosphere control at scale for engineering application.

5. Conclusions

This paper reinterprets the problem of refractory high-sulfur iron tailings as a search for a common operating state rather than a competition between opposing atmospheres, and it uses coupled thermodynamic, kinetic and mass-balance analysis, without experimental validation, to map out where such a state exists and how far it can be realized. The work shows that the incompatibility between desulfurization and magnetization disappears in a narrow low-oxygen window; at this time, the sulfur released by pyrite decomposition, together with the CO released by siderite, acts as an internal reducing agent to transport hematite to magnetite, and sulfur escapes as gaseous oxides, with microwave selective heating serving as a suitable energy source for the reactive phase. The feasibility domain contracts with rising temperature, from 8.8 decades of oxygen partial pressure at 500 °C to 2.8 decades at 700 °C; therefore, aggressive heating is employed in the limited margin before over-reduction occurs, and a closed-material-balance approach is used to establish a firm upper bound for magnetite-associated iron (31.38 g per 100 g of feed) and attainable recovery (81.6%), as calculated in the analysis report, rather than optimizing for a target. The tension between further sulfur removal and magnetite yield is the controlling trade-off: at least 95.6% of the sulfur retained in magnetic pyrrhotite must be removed in a second stage to reach 0.10% S, and it is presented as a boundary envelope because the coupling between further sulfur removal and over-reduction loss cannot be determined by any available rate function. The value of these results is to provide boundary criteria that delimit the realistic operating region and to support a justifiable performance expectation rather than an optimistic forecast, so that the feasibility of the proposed route rests on internally consistent thermodynamic and mass-balance limits. Realizing the scheme in practice will require quantifying the second-stage kinetics under controlled low-oxygen conditions and demonstrating stable atmosphere control at scale, so that the theoretical account developed here can be converted into a validated process—possibly with an additional reducing agent—while recovering the resource value carried by the tailings.

References

[1] Long H, Zhu D, Pan J, Li S, Yang C, Guo Z, et al. A critical review on metallurgical recovery of iron from iron ore tailings. J Environ Chem Eng. 2024;12(2):112140. https://doi.org/10.1016/j.jece.2024.112140

[2] Wu W, Kang K, Ye Q, Luo A, Zhang J, Wang J, et al. Comprehensive utilization of iron ore tailings: a review of sustainable practices and technologies. Min Metall Explor. 2026;43(1):413-430. https://doi.org/10.1007/s42461-025-01443-6

[3] Qiu G, Ning X, Shen J, Wang Y, Zhang D, Deng J. Recovery of iron from iron tailings by suspension magnetization roasting with biomass-derived pyrolytic gas. Waste Manag. 2023;156:255-263. https://doi.org/10.1016/j.wasman.2022.11.034

[4] Shamase A, Nheta W, Mulaba-Bafubiandi AF. Beneficiation of low-grade iron plant tailings through magnetization roasting using macadamia nutshell reductant. J Sustain Metall. 2025;11(3):2371-2392. https://doi.org/10.1007/s40831-025-01106-2

[5] Jia Z, Yang B, Zhang B, Yan G, Luo G, Xie Y, et al. Desulfurization mechanism of high-sulfur iron concentrate pellets during oxidative roasting. Metals. 2026;16(3):306. https://doi.org/10.3390/met16030306

[6] Bobadilla-Fazzini RA, Poblete-Castro I. Establishing a green biodesulfurization process for iron ore concentrates in stirred tank and leaching column bioreactors using Acidithiobacillus thiooxidans. Front Bioeng Biotechnol. 2023;11:1324417. https://doi.org/10.3389/fbioe.2023.1324417

[7] Yu J, Han Y, Gao P, Li Y, Yuan S, Li W. An innovative methodology for recycling iron from magnetic pre-concentrate of an iron ore tailing. Physicochem Probl Miner Process. 2018;54(3):668-676. https://doi.org/10.5277/ppmp1863

[8] Niyonzima JC, Luo L, Xie H, Wang H, Ndayiragije T, Ntiharirizwa S. Effective sulfur removal mechanism of a refractory S-Pb-Zn-bearing hematite ore through a sustainable oxidation-roasting process. J Sustain Metall. 2025;11(2):1465-1481. https://doi.org/10.1007/s40831-025-01023-4
[9] Kukkala PC, Kumar S, Nirala A, Khan MA, Alkahtani MQ, Islam S. Beneficiation of low-grade hematite iron ore fines by magnetizing roasting and magnetic separation. ACS Omega. 2024;9(7):7634-7642. https://doi.org/10.1021/acsomega.3c06802
[10] Yu J, Sun H, Li P, Han W, Li Y, Han Y. A pilot study on recovery of iron from sulfur-bearing hematite ore using hydrogen-based mineral phase transformation followed by magnetic separation. J Environ Chem Eng. 2023;11(5):110630. https://doi.org/10.1016/j.jece.2023.110630
[11] Zhao Q, Xue J, Chen W. Mechanism of improved magnetizing roasting of siderite-hematite iron ore using a synergistic CO-H_2 mixture. J Iron Steel Res Int. 2020;27(1):12-21. https://doi.org/10.1007/s42243-019-00242-w
[12] Chen J, Li X, Gao L, Guo S, He F. Microwave treatment of minerals and ores: heating behaviors, applications, and future directions. Minerals. 2024;14(3):219. https://doi.org/10.3390/min14030219
[13] Kingman SW. Recent developments in microwave processing of minerals. Int Mater Rev. 2006;51(1):1-12. https://doi.org/10.1179/174328006X79472
[14] Boyabat N, Özer AK, Bayrakçeken S, Gülaboğlu MŞ. Thermal decomposition of pyrite in the nitrogen atmosphere. Fuel Process Technol. 2004;85(2-3):179-188. https://doi.org/10.1016/S0378-3820(03)00196-6
[15] Aracena A, Jerez O. Mechanism and kinetics of pyrite transformation at elevated temperatures. Physicochem Probl Miner Process. 2021;57(6):131-143. https://doi.org/10.37190/ppmp/143124
[16] Chen X, Zhao N, Li Z, Wang Z. Study on the migration and release of sulfur during the oxidizing roasting of high-sulfur iron ore. Minerals. 2024;14(3):276. https://doi.org/10.3390/min14030276
[17] Zhu X, Han Y, Sun Y, Gao P, Li Y. Thermal decomposition of siderite ore in different flowing atmospheres: phase transformation and magnetism. Miner Process Extr Metall Rev. 2023;44(3):201-208. https://doi.org/10.1080/08827508.2022.2040498
[18] Metaxas AC, Meredith RJ. Industrial microwave heating. London: Peter Peregrinus; 1983.
[19] Komarov V, Wang S, Tang J. Permittivity and measurements. In: Chang K, editor. Encyclopedia of RF and microwave engineering. New York: Wiley; 2005. p. 3693-3711. https://doi.org/10.1002/0471654507.eme308
[20] Hu G, Dam-Johansen K, Wedel S, Hansen JP. Decomposition and oxidation of pyrite. Prog Energy Combust Sci. 2006;32(3):295-314. https://doi.org/10.1016/j.pecs.2005.11.004
[21] McBride BJ, Zehe MJ, Gordon S. NASA Glenn coefficients for calculating thermodynamic properties of individual species. Cleveland (OH): NASA Glenn Research Center; 2002. Report No.: NASA/TP-2002-211556.
[22] Hunt CP, Moskowitz BM, Banerjee SK. Magnetic properties of rocks and minerals. In: Ahrens TJ, editor. Rock physics and phase relations: a handbook of physical constants. Washington (DC): American Geophysical Union; 1995. p. 189-204. (AGU Reference Shelf; vol. 3). https://doi.org/10.1029/RF003p0189
[23] Svoboda J, Fujita T. Recent developments in magnetic methods of material separation. Miner Eng. 2003;16(9):785-792. https://doi.org/10.1016/S0892-6875(03)00212-7
[24] Li W, Chen J, Zhou W, Han Y, Shan Y. Effect of bastnaesite as reductant on hematite reduction during in-situ suspension magnetization roasting of refractory iron ore under neutral atmosphere. Int J Min Sci Technol. 2022;32(4):877-886. https://doi.org/10.1016/j.ijmst.2022.03.009
[25] Zhang Q, Sun Y, Han Y, Gao P, Li Y. Thermal decomposition kinetics of siderite ore during magnetization roasting. Min Metall Explor. 2021;38(3):1497-1508. https://doi.org/10.1007/s42461-021-00417-8
[26] Zhang Q, Sun Y, Qin Y, Gao P, Yuan S. Siderite pyrolysis in suspension roasting: an in-situ study on kinetics, phase transformation, and product properties. J Cent South Univ. 2022;29(6):1749-1760. https://doi.org/10.1007/s11771-022-5059-9
[27] Xie L, Hao J, Hu C, Zhang H. Study on magnetization roasting kinetics of high-iron and low-silicon red mud. Materials. 2023;16(18):6178. https://doi.org/10.3390/ma16186178
[28] Zhang Q, Sun Y, Han Y, Li Y, Gao P. Producing magnetite concentrate via self-magnetization roasting in N_2 atmosphere: phase and structure transformation, and extraction kinetics. J Ind Eng Chem. 2021;104:571-581. https://doi.org/10.1016/j.jiec.2021.09.008
[29] Zhou W, Sun Y, Han Y, Gao P, Li Y. Recycling iron from oolitic hematite via microwave fluidization roasting and magnetic separation. Miner Eng. 2021;164:106851. https://doi.org/10.1016/j.mineng.2021.106851
[30] Tang X, Chen Y. A review of flotation and selective separation of pyrrhotite: a perspective from crystal structures. Int J Min Sci Technol. 2022;32(4):847-863. https://doi.org/10.1016/j.ijmst.2022.06.001
[31] King MJ, Davenport WG, Moats MS. Sulfuric acid manufacture: analysis, control and optimization. 2nd ed. Amsterdam: Elsevier; 2013. https://doi.org/10.1016/C2011-0-05490-X

[32] Haque KE. Microwave energy for mineral treatment processes—a brief review. Int J Miner Process. 1999;57(1):1-24. https://doi.org/10.1016/S0301-7516(99)00009-5
[33] Sun H, Zou Z, Zhang M, Yan D. Fluidized magnetization roasting of refractory siderite-containing iron ore via preoxidation-low-temperature reduction. Int J Miner Metall Mater. 2023;30(6):1057-1066. https://doi.org/10.1007/s12613-022-2576-3
[34] Yuan S, Wang R, Zhang Q, Li Y, Gao P. Extraction and phase transformation of iron in fine-grained complex hematite ore by suspension magnetizing roasting and magnetic separation. Korean J Chem Eng. 2022;39(7):1891-1901. https://doi.org/10.1007/s11814-022-1116-1